PERGAMON

International Journal of Heat and Mass Transfer 45 (2002) 3503–3516

International Journal of HEAT and MASS TRANSFER

www.elsevier.com/locate/ijhmt

An immersed-boundary method for the dynamics of premixed flames

K.L. Pan [a], W. Shyy [b,*], C.K. Law [a]

[a] Department of Mechanical and Aerospace Engineering, Princeton University, Princeton, NJ 08544, USA
[b] Department of Aerospace Engineering, Mechanics and Engineering Science, University of Florida, 231 Aerospace Building, P.O. Box 116250, Gainesville, FL 32611-6250, USA

Received 6 December 2001; received in revised form 7 February 2002

Abstract

The accuracy of the immersed-boundary method is investigated for the simulation of the propagation of a premixed flame, characterized by sharp and moving interfaces separating unburned and burned gases with disparate fluid properties. In particular, the spurious pressure fields observed when employing the cosine weighting function in previous studies are found to be caused by the non-conservation in the interfacial region, and are removed in the present study by using area weighting. Furthermore, the sensitivity of the front propagation velocity to the movement and location of the flame, characterized by a discontinuous velocity profile, is substantially moderated by the use of an improved technique based on known immersion distribution. The improved performance of the present method is demonstrated through the evolution of the Darrieus–Landau instability.

1. Introduction

Numerical simulation of flows with moving boundaries needs to identify the shape, location, and movement of the interface in the course of computation. The problem is a challenging one, especially for situations in which properties change substantially across the interface, the interface geometry evolves drastically, and the front dynamics depends on the properties of the interface such as its curvature and variable gradient. A number of techniques, including those of Lagrangian, Eulerian, and mixed Eulerian–Lagrangian, have been developed, as documented in, for example, [9,16,21–24,26,29] and [1]. Prominent among them is the immersed-boundary method, originally developed by Peskin [17] and subsequently adopted, extended, and applied by others [1,5,10,25,27]. This method is based on the mixed Eulerian–Lagrangian approach, and incorporates interfacial conditions into the governing field equations by introducing additional source terms. Various aspects of the immersed-boundary method have been discussed, including the basic analysis and accuracy assessment [3,11,18]. While the interface thickness is zero in the context of continuum formulation, in the immersed-boundary method the interface is numerically smeared out. To ensure that the computational strategy is fundamentally sound, overall conservation, such as that of mass, cannot be affected by the interface smearing. In addition, the jump conditions across the sharp interface must be satisfied globally, if not at the exact location of the interface.

The immersed-boundary method has been extensively applied to the study of drop and bubble dynamics [10,25–27], for which a key issue is the representation of surface tension by some suitable kernels [2,28]. With surface tension smoothed out by the discrete δ-function and converted to a body force term, the governing equations can be solved for the entire domain without explicitly separating the different phases. Recently this method has also been applied to the dynamics of flames [19], for which a flame surface separates two media with distinct fluid properties such as density and viscosity. The key interfacial property here is the mass exchange due to combustion, expressed in the form of a divergence operator. The solution of Qian et al. [19] accounts

* Corresponding author. Tel.: +1-352-392-0961; fax: +1-352-392-7303.
E-mail address: wei-shyy@ufl.edu (W. Shyy).

0017-9310/02/$ - see front matter
PII: S0017-9310(02)00075-3

Nomenclature

d_j	smoothing function in 1-D
H	Heaviside step function
k	wave number
p	pressure
q	density ratio of unburned to burned gases
r	distance between the flame and specific grid line
s_{ave}	average burning speed
s_{u}	laminar burning velocity
t	time
$\mathbf{u}$	flow velocity vector
u_{ave}	average flow velocity at the flame front
u_{in}	inlet flow velocity for 1-D propagation
u_{u}	flow velocity at the upstream boundary of the front
V_f	normal propagation velocity of the flame
$\mathbf{x}$	position vector

Greek symbols

Ω	computational domain
ρ	density
μ	viscosity
τ_{ij}	stress tensor
$\omega_{i,j}$	smoothing function in 2-D
φ	field variable treated by the immersed-boundary method

for the density jump as well as the evaluation of curvature which affects the burning velocity of the flame. We now extend this study by investigating two issues that have not been adequately resolved, namely: (i) unsteady pressure evolution, and (ii) computation of the interface velocity. As will be demonstrated, a satisfactory resolution of these issues is critical for the successful computation of the flame dynamics.

We note in passing that Noh and Woddward [15], and Chorin [4], have developed the simple line interface calculation (SLIC) method to track a thin flame front of arbitrary shape, in which a marker function is advected with the flow, while Helenbrook et al. [8] have advanced a numerical algorithm describing the dynamics of a flame surface without artificial smearing. Recently, Nguyen et al. [14] have adopted a boundary condition capturing technique, based on the level set method [22] and ghost fluid method [6], to simulate the motion of premixed flames, in which no special treatment is required for the merging of flame fronts. All these methods merit further development.

2. Numerical approach

The governing equations of continuity and momentum for the flow field are [19]:

$$\begin{aligned} &\frac{\partial \rho}{\partial t} + \nabla \cdot \rho \mathbf{u} = 0, \\ &\frac{\partial \rho \mathbf{u}}{\partial t} + \nabla \cdot \rho \mathbf{u}\mathbf{u} = -\nabla p + \nabla \cdot \overline{\overline{\tau_{ij}}}, \\ &\overline{\overline{\tau_{ij}}} = \mu(\nabla \mathbf{u} + \nabla^{\mathrm{T}} \mathbf{u}). \end{aligned} \tag{1}$$

The procedure to solve the Navier–Stokes equations follows the projection method described in [20], with

$$\frac{(\rho \mathbf{u})^{n+1} - (\rho \mathbf{u})^{*}}{\Delta t} = -\nabla_h p^{n+1}, \tag{2}$$

where the unprojected mass flux is defined as

$$(\rho \mathbf{u})^{*} = (\rho \mathbf{u})^{n} - \Delta t \left[\nabla_h \cdot (\rho \mathbf{u}\mathbf{u})^{n} + \nabla_h \cdot \overline{\overline{\tau_{ij}^{n}}} \right]. \tag{3}$$

Taking divergence on both sides yields the Poisson equation for pressure

$$\nabla_h^2 p^{n+1} = \frac{\nabla_h \cdot (\rho \mathbf{u})^{*} - \nabla_h \cdot (\rho \mathbf{u})^{n+1}}{\Delta t}. \tag{4}$$

Here the subscript h and the superscript n, respectively, refer to the discretizations in space and time. A staggered mesh as used in the MAC scheme [7] is employed.

To solve the pressure field, the divergence of the mass flux, $\nabla_h \cdot (\rho \mathbf{u})^{n+1}$, needs to be determined at each time step. It appears as a source term at the interface, similar to the role of surface tension in two-phase flows [28], and can be expressed by a numerically approximated δ-function. The jump condition of a flow variable is then expressed by the Heaviside step function, which in two-dimension is

$$H(x,y) = \int_A \delta(x - x')\delta(y - y')\,\mathrm{d}a' \tag{5}$$

with its gradient given by

$$\nabla H(x,y) = -\oint_L \delta(x - x')\delta(y - y')\,\mathrm{d}l'. \tag{6}$$

The divergence of mass flux can then be obtained through the continuity equation

$$\nabla \cdot \rho \mathbf{u} = -\frac{\partial \rho}{\partial t} = -\Delta\rho \int_f \delta(\mathbf{x} - \mathbf{x}_f) V_f \,\mathrm{d}l \tag{7}$$

in which $\Delta\rho$ is the density difference between unburned and burned gases, and V_f the normal propagation speed of the flame front at position $\mathbf{x}_f$. The integration is carried out along the flame interface.

2.1. Finite δ-function

In the immersed-boundary method, the δ-function is approximated by broadening its base to several grid points, with the constraint that geometric conservation given by $\int_{-\infty}^{+\infty}\delta(x-x_f)\,\mathrm{d}x=1$ is satisfied. The corresponding discrete form is

$$h\sum_{\Gamma} d_j(x_j-x_f)=1, \tag{8}$$

where Γ is the support region for the smoothing function $d_j(r)$ and h is the grid size. The smoothed property per unit area can then be evaluated as

$$\varphi_a(x_f)=\int_{\Delta s}\varphi_l(x)\delta(x-x_f)\,\mathrm{d}l \tag{9}$$

and the corresponding numerical approximation yields

$$\hat{\varphi}_{i,j}(x_{i,j})=h\sum_{\Delta s}\hat{\varphi}_l(l)\omega^l_{i,j}(x_{i,j}-x_f)\Delta l. \tag{10}$$

The "∧" above a variable refers to an approximate value and Δs is a small segment within the specific area. There are various ways to choose the finite delta function, $d_j(r)$. Qian et al. [19] adopted the cosine smoothing function proposed by Peskin [17]

$$\omega^l_{i,j}=d_i(x_f-ih)d_j(y_f-jh),$$
$$d(r)=\begin{cases}(1/4h)[1+\cos(\pi r/2h)], & |r|\leqslant 2h,\\ 0, & |r|\geqslant 2h.\end{cases} \tag{11}$$

The summation of weights for all four points in the immersed region satisfies Eq. (8).

2.2. Estimation of flame velocity

The flame propagation velocity can be evaluated by $V_f=s_\mathrm{u}+u_\mathrm{u}$, where s_u and u_u, respectively, represent the (laminar) burning velocity defined with respect to the unburned mixture, and the flow velocity at the upstream boundary of the front. The laminar burning velocity is a function of the thermodynamic state of the unburned mixture, while the flow velocity at the flame front needs to be determined from the calculated flow field. Fig. 1 illustrates the problem under study, in which $s_\mathrm{b}+u_\mathrm{b}=s_\mathrm{u}+u_\mathrm{u}$ and the index "b" designates the burned side.

Following [19], a "lumped" expression for flame propagation

$$V_f=u_\mathrm{u}-s_\mathrm{u}=u_\mathrm{ave}-s_\mathrm{ave} \tag{12}$$

is used, in which the average flow velocity u_ave is estimated from

$$u_\mathrm{ave}=\frac{\rho_\mathrm{u}u_\mathrm{u}+\rho_\mathrm{b}u_\mathrm{b}}{\rho_\mathrm{u}+\rho_\mathrm{b}} \tag{13}$$

such that

$$s_\mathrm{ave}=u_\mathrm{ave}-u_\mathrm{u}+s_\mathrm{u}=\frac{\rho_\mathrm{b}(u_\mathrm{b}-u_\mathrm{u})}{\rho_\mathrm{u}+\rho_\mathrm{b}}+s_\mathrm{u}. \tag{14}$$

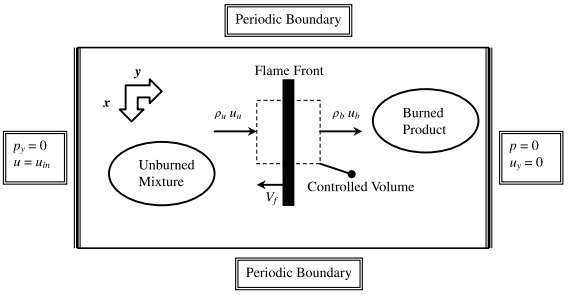

Fig. 1. A simplified illustration of flame propagation. The propagation velocity at a sharp interface can be evaluated by: $V_f=s_\mathrm{u}+u_\mathrm{u}=s_\mathrm{b}+u_\mathrm{b}$, where s_u and u_u represent the (laminar) burning velocity and the local flow velocity exactly upstream of the front, respectively. The indices "a" and "b ", respectively, refer to the unburned and burned sides of the flame.

From mass conservation across the flame, one obtains

$$\rho_\mathrm{u}s_\mathrm{u}=\rho_\mathrm{b}s_\mathrm{b}=\rho_\mathrm{b}(u_\mathrm{b}-V_f)=\rho_\mathrm{b}(u_\mathrm{b}-u_\mathrm{u}+s_\mathrm{u}), \tag{15}$$

which yields

$$s_\mathrm{u}=\frac{\rho_\mathrm{b}(u_\mathrm{b}-u_\mathrm{u})}{\rho_\mathrm{u}-\rho_\mathrm{b}}. \tag{16}$$

Consequently, the corresponding average flame speed is given by

$$s_\mathrm{ave}=\frac{2\rho_\mathrm{u}s_\mathrm{u}}{\rho_\mathrm{u}+\rho_\mathrm{b}}=\frac{\rho_\mathrm{u}s_\mathrm{u}}{\rho_\mathrm{ave}}. \tag{17}$$

Since the flame is a discontinuity, the velocity and density fields are also discontinuous. Thus care is needed in interpolating u_ave across the flame front; otherwise, substantial numerical error can arise. In particular, as will be demonstrated later, the divergence of the mass flux, which is a source in the Poisson equation for the pressure field, is sensitive to the interpolation error.

In the following, we present a theoretical analysis as well as an improved numerical procedure for computation of the pressure field and the rate of flame propagation.

3. Pressure computation

3.1. Diagnosis

For simplicity, we consider a periodic flow to highlight the issues of interest here. The boundary conditions in the y-direction are $p_y(0)=0$ and $p(1)=0$ in $[0,1]$, as marked in Fig. 1, together with the velocity boundary conditions $u(0)=u_\mathrm{in}$ and $u_y(1)=0$. In the x-direction, periodic boundary condition is imposed. In an unbounded domain, density, velocity, and pressure change abruptly across the flame front, and for a stationary flame, the computed dependent variables follow globally

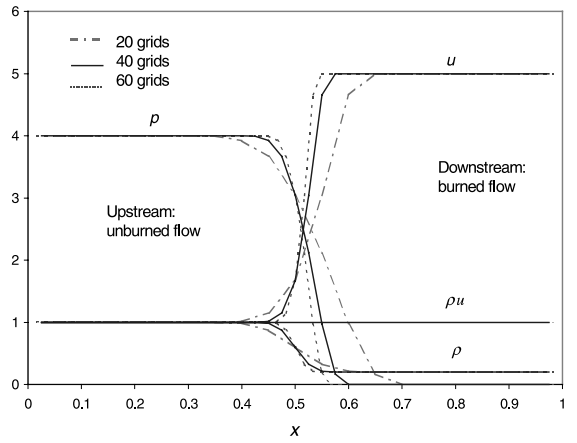

Fig. 2. Computational profiles across a flame front are depicted for pressure, velocity, density, and mass flux. Steady pressure distribution is maintained as the flame motion is counteracted by the incoming flow; it remains stationary in time. The thickness of the immersed boundary shrinks as the mesh resolution improves.

the Rankine–Hugoniot relation, as shown in Fig. 2. The numerical solution becomes sharper as the grid resolution improves, which reduces the thickness of the immersed boundary region. However, as respectively shown in Figs. 3(a) and (b), the pressure across the flame front exhibits spurious oscillations if the flame is treated as a moving object in the computational domain, while the velocity field remains well behaved. These results suggest that evaluation of the source term in the Poisson equation for pressure, Eq. (4), i.e., the divergence of the mass flux, should be examined more carefully. To further demonstrate this error, we employ the analytical value of the interface velocity to compute the divergence of the mass flux in the pressure equation, so as to exclude the error from interpolation, and to test the smoothing accuracy. As shown in Fig. 4(a), with the cosine weighting function, spurious, periodic profiles in the pressure field are manifested. However, if we adopt an area (linear) weighted formula

$$d(r) = \begin{cases} \frac{1}{h}(1 - |r|/h), & |r| \leqslant h, \\ 0, & |r| \geqslant h \end{cases} \tag{18}$$

satisfying the geometric conservation law, Eq. (8), the resulting pressure distribution is well behaved, as shown in Fig. 4(b). To explain the reasons behind the differences observed between the two weighting functions, we next present a formal analysis.

3.2. Analysis

The approach is similar to that of Beyer and LeVeque [3], except that a discontinuous velocity profile across the flame interface, instead of a continuous profile, is considered. The flame is assumed to be initially situated in a quiescent environment such that the divergence of mass flux caused by the flame front generates the non-uniform pressure field. In the projection method, with advection ($\nabla \cdot \rho\mathbf{uu}$) across the flame in the velocity field, a revised pressure distribution is established.

Consider the Poisson equation for pressure, Eq. (4), for an initially quiescent flow. The pressure field subsequently generated is described by

$$\nabla^2 p = -\frac{\nabla \cdot (\rho\mathbf{u})^{n+1}}{\Delta t} = \Delta\rho \int_f \delta(x - x')\delta(y - y')V_f \, \mathrm{d}l'. \tag{19}$$

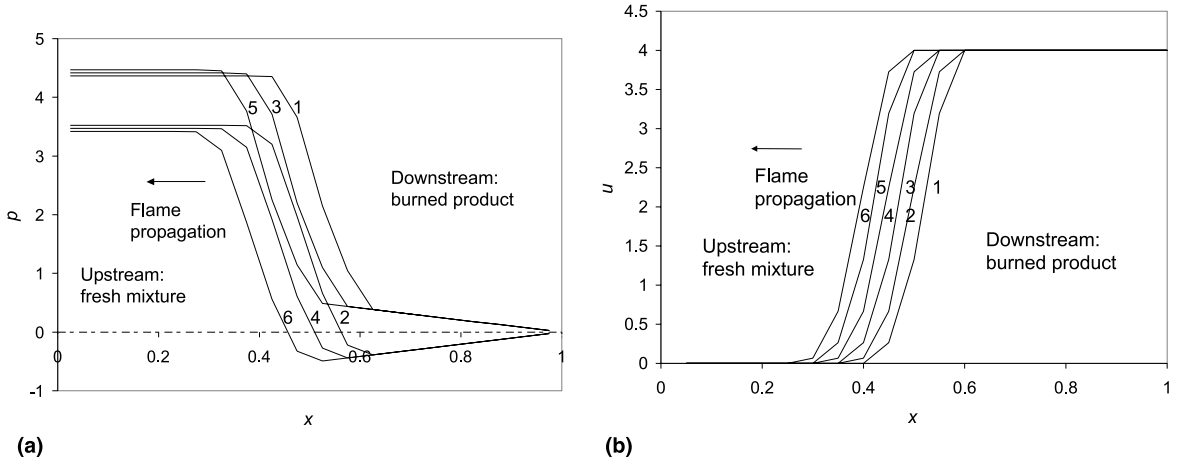

Fig. 3. Pressure and velocity profiles associated with a flame front moving from the right to the left with quiescent unburned gas. The corresponding time of symbols 1–6 are $t = 0.025$, 0.05, 0.075, 0.1, 0.125, and 0.15. (a) The pressure fluctuates as the front location relative to grid lines. (b) Since an exact pressure gradient on either side of the flame can be retrieved, due to conservative weighting, the velocity is accurate away from the immersed boundary and the difference across the flame is constant.

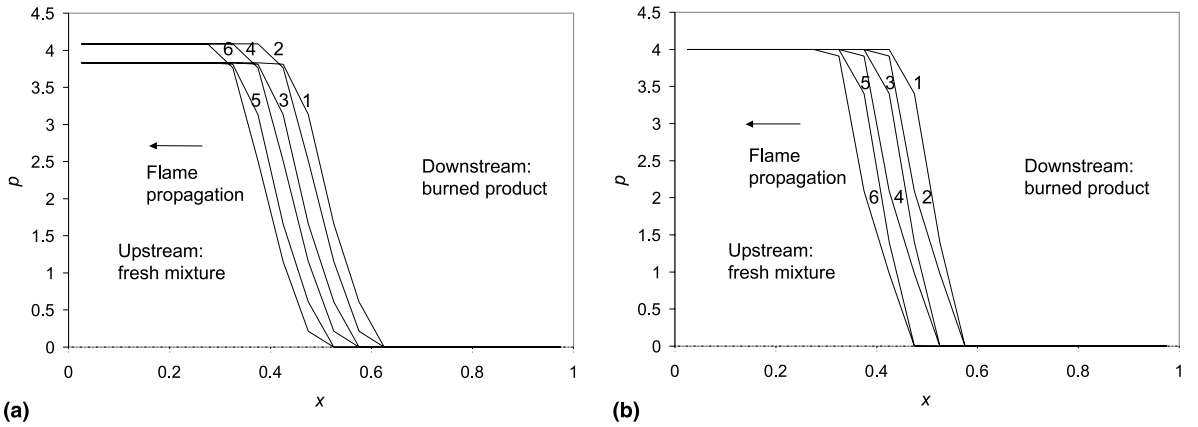

Fig. 4. The pressure profile associated with a flame front moving from the right to the left with quiescent unburned gas. The solutions are shown with equal time increment of 0.025. The analytical value of the propagation velocity is employed. (a) The cosine weighting function causes the upstream pressure fluctuates periodically as the front position relative to grid line changes. (b) The area weighting causes the pressure difference across the flame to remain steady.

For the one-dimensional condition, it is

$$\frac{\mathrm{d}^2 p}{\mathrm{d}x^2} = \alpha\delta(x - x_f), \tag{20}$$

where $\alpha \equiv V_f \Delta\rho$ and x_f is the location of the flame front. In the immersed-boundary method, the δ-function is approximated by discrete sources $d_j(r)$ spread over several grid points. Eq. (20) then becomes

$$d_x^2 \hat{p}_j = \alpha d_j(x_j - x_f). \tag{21}$$

The original differential Eq. (20) can be solved analytically by Green's function $G(x;a)$, satisfying $(p_{xx}, G) = (p, G_{xx}) = p(x)$ with suitable boundary conditions

$$p(x) = \alpha \int_\Omega G(x';x)\delta(x' - x_f)\,\mathrm{d}x' = G(x;x_f). \tag{22}$$

The boundary conditions for G with $p_x(0) = 0$ and $p(1) = 0$ in the domain $[0,1]$ are $G_x(0) = 0$ and $G(1) = 0$. The solution is

$$G(x;a) = \begin{cases} -(1-a), & x \leqslant a, \\ -(1-x), & x \geqslant a \end{cases} \tag{23}$$

such that

$$G_x(x;a) = H(x-a),$$

$$G_{xx}(x;a) = \delta(x-a).$$

Numerically, the corresponding approximation is

$$\hat{p}_j(x_j) = \alpha h \sum_k G(x_k;x_j) d_k(x_k - x_f) = \alpha \hat{G}(x_j;x_f). \tag{24}$$

The truncation error can be estimated by comparing Eqs. (22) and (24). We can expand $G(x_k;x_j)$ in Eq. (24) around x_f, accounting for the jump in $G_x(x_j;x_f)$ expressed by the Heaviside function.

If the geometric conservation law represented by Eq. (8) is satisfied for $d_j(x_j - x_f)$, then, after some manipulation, the truncation error is given by

$$\begin{aligned} E_{\mathrm{p}}^{\mathrm{I}}(x_j) &= \hat{p}_j(x_j) - p(x_j) \\ &= \alpha h \sum_k [G(x_f;x_j) + G_x(x_k;x_j)(x_k - x_j) \\ &\quad + G_x(x_f;x_j)(x_j - x_f)] d_k(x_k - x_f) - \alpha G(x_j;x_f) \\ &= \alpha h \sum_k [G_x(x_k;x_j)(x_k - x_j) + G_x(x_f;x_j) \\ &\quad \times (x_j - x_f)] d_k(x_k - x_f) \\ &= \alpha h \sum_k [H(x_k - x_j)(x_k - x_j) + H(x_f - x_j) \\ &\quad \times (x_j - x_f)] d_k(x_k - x_f). \end{aligned} \tag{25}$$

External to the immersed boundary, that is, $|x_j - x_f| \geqslant \lambda h$, where λh is the support area for the discrete source $d_j(x_j - x_f)$ which diminishes outside the boundary, the summation inside the bracket of Eq. (25) yields $x_k - x_f$ upstream of the flame ($x_j - x_f \leqslant \lambda h$), and zero downstream of the flame ($x_j - x_f \geqslant \lambda h$).

Fig. 5 illustrates the main features of the above analysis. At this stage, the immersed boundary smoothed by the cosine weighting function is inherited with an error of order h. Furthermore, the magnitude of the error depends on the relative position of the front within a computational cell. Outside the immersed boundary region, the error appears in the upstream of the flame front (Fig. 5(a)) where the Neumann boundary condition is assigned at the inlet. It is noted that the pressure on the right boundary is fixed while that on the left side is determined by integrating the pressure gradient across the flame. The periodic behavior in Fig. 5(b) is revealed

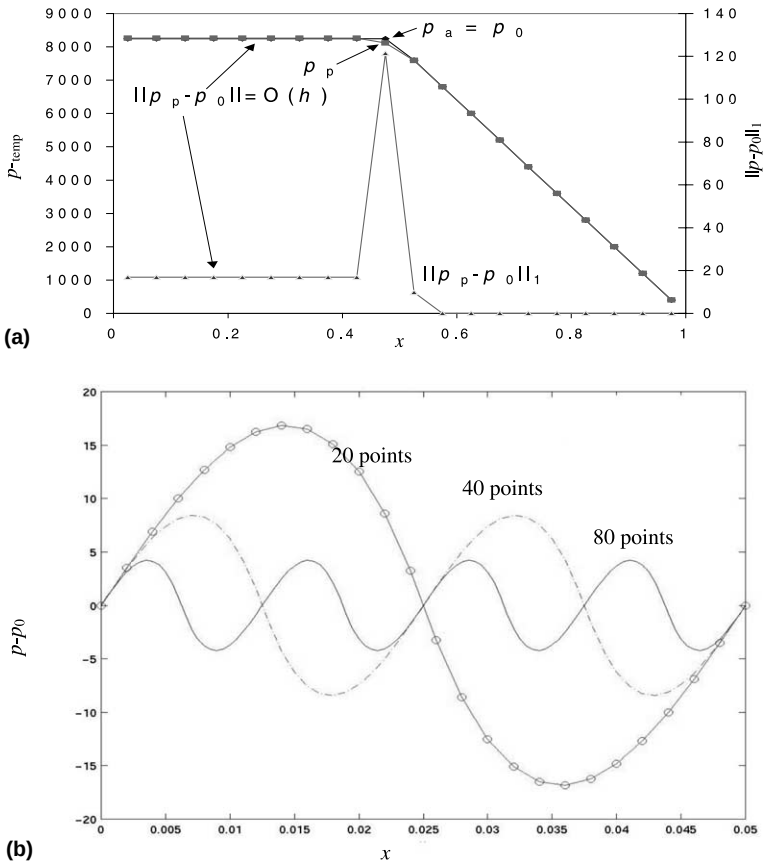

Fig. 5. Computed pressure characteristics with different weighting functions. (a) The pressure ramp is computed exactly with area weighting ($p_a = p_0$) while the cosine weighting function renders an error of O(h) in the left plane. (b) Periodic errors of the pressure in the left plane is O(h) with cosine weighting.

from Eq. (25), in which the error is reduced by half when the number of grid points is doubled. This indicates that the error is O(h). On the other hand, the exact solution can be obtained using the area weighting function, Eq. (18), since its linear compensation leads to

$$\sum_{k=1}^{2}(x_k - x_f)d_k(x_k - x_f) = 0. \tag{26}$$

The error shown in Eq. (25) thus becomes zero. The above analysis establishes that an error arising from the smoothing procedure can significantly affect the accuracy of the solution. With this background, issues related to the pressure computation are discussed next.

3.2.1. Local acceleration of fluid element due to transient pressure driving

The initial pressure ramp just described causes local acceleration of the fluid element. Since the initial velocity is zero and there is no advection, the momentum equation at this step becomes

$$\frac{\hat{\rho}\hat{u}_j^1 - \hat{\rho}\hat{u}_j^0}{\Delta t} = -d_x\hat{\boldsymbol{p}}_j, \tag{27}$$

where $\hat{\rho}\hat{u}_j^0 = 0$. The error associated with the computed p_j is transmitted to u_j by

$$\|\hat{\rho}\hat{u}_j - \rho u(x_j)\|_1 = \Delta t \cdot \left\| d_x\hat{\boldsymbol{p}}_j - \frac{\mathrm{d}p}{\mathrm{d}x}(x_j) \right\|_1. \tag{28}$$

Here the analytical pressure gradient can be expressed by a step function

$$\frac{\mathrm{d}p}{\mathrm{d}x}(x) = \alpha H(x - x_f) = \alpha \int_\Omega H(x - x')\delta(x' - x_f)\,\mathrm{d}x' \tag{29}$$

with the discrete form being

$$d_x\hat{\boldsymbol{p}}_j(x_j) = \alpha h \sum_k H(x_j - x_k)d_k(x_k - x_f). \tag{30}$$

The error induced by the immersed boundary treatment is then evaluated as

$$E_{\mathrm{p}}^{\mathrm{II}}(x_j) = d_x\hat{\boldsymbol{p}}_j(x_j) - \frac{\mathrm{d}p}{\mathrm{d}x}(x_j)$$
$$= \alpha h \sum_k H(x_j - x_k) d_k(x_k - x_f) - \alpha H(x_j - x_f)$$
$$= \alpha h \sum_k [H(x_j - x_k) - H(x_j - x_f)] d_k(x_k - x_f). \tag{31}$$

Eq. (31) indicates that an error of O(1) in the pressure gradient is generated within the immersed area, whose magnitude varies with the front position relative to the grid lines. The error is then propagated by the mass flux, as shown in Eq. (28). It is noted that the pressure gradient external to the immersed boundary region is exact for any smoothing function satisfying Eq. (8) because the conservation of discrete sources in the Poisson equation for pressure, Eq. (21), recovers the analytical jump condition. Therefore the mass flux can be calculated correctly on both sides of the flame, with smooth transition in the flame region. Consequently, the velocity difference across the flame front can be retrieved accurately to that held by a sharp interface and is not affected by the flame motion, as shown in Fig. 3(b).

3.2.2. Final balanced state for momentum conservation

The final pressure field can be obtained by balancing the pressure with the well-evolved velocity field as mentioned. Neglecting viscous and body forces, the momentum equation resumes the original nonlinear form

$$\frac{\partial \rho u}{\partial t} + \frac{\partial \rho u^2}{\partial x} = -\frac{\partial p}{\partial x} \tag{32}$$

through which the error for the pressure computation can be estimated. The jump condition across the flame front can be recovered by direct integration of Eq. (32)

$$\frac{\partial}{\partial t}\int_{-\lambda h}^{+\lambda h} \rho u \,\mathrm{d}x + \Delta \rho u^2 = -\Delta p = p_{\mathrm{u}} - p_{\mathrm{b}}. \tag{33}$$

Since the second term can be calculated exactly, as elucidated in 3.2.1, the error in the pressure difference is induced by the first integration

$$E_{\mathrm{p}}^{\mathrm{III}}(x_j) = \Delta\hat{\boldsymbol{p}}_j(x_j) - \Delta p(x_j)$$
$$= \frac{\partial}{\partial t}\int_{-\lambda h}^{+\lambda h} (\rho u - \hat{\rho}\hat{\boldsymbol{u}})\,\mathrm{d}x$$
$$= -\alpha h \Delta t \frac{\partial}{\partial t}\int_{-\lambda h}^{+\lambda h} \sum_k [H(x_j - x_k) - H(x_j - x_f)] d_k(x_k - x_f)\,\mathrm{d}x. \tag{34}$$

The integral in Eq. (34) represents the difference in the underlying areas between the theoretical step profile and the immersed distribution of the mass flux (or the pressure gradient, related by Eq. (28)) in the ρu versus x plot (or ∇p versus x), which is O(h) after combining with the coefficient h in the expression. Consequently, for O($1/h$) temporal variation, the computational error in the pressure jump becomes O(1) if the cosine smoothing function is adopted, with the magnitude varying with the relative front position in a computational cell. This analysis is supported by Fig. 6, and provides an explanation for the evidence of oscillations shown in Fig. 4(a). However, when area weighting is used, such an error is not introduced because the temporal variation of the integral in Eq. (34) becomes zero, as shown in Fig. 4(b).

3.3. Conservation in the immersed boundary region

As illustrated in Eq. (21), if the discrete source $d_j(r)$ satisfies Eq. (8), the pressure gradient determined from the immersed-boundary method can recover the analytical values on both sides of the flame front. The pressure jump, however, depends on the integration of the pressure gradient through the transition layer and is closely related to the distributed shape. Area weighting can preserve the global pressure variation because the weight of the smoothed source at the grid point ahead of the flame, multiplied by the distance of its region of influence, is identical to that of its counterpart grid point behind the flame, as implied by Eq. (26). The integral hence recovers the exact value described by a step function. One can easily demonstrate this from the geometric conservation for the distributed area in the $\nabla p - x$ relation. Specifically

$$\Delta p_{\mathrm{linear}} = \int_{-\lambda h}^{f} \frac{\mathrm{d}p}{\mathrm{d}x'}\mathrm{d}x' + \int_{f}^{+\lambda h} \frac{\mathrm{d}p}{\mathrm{d}x'}\,\mathrm{d}x'$$
$$= \frac{1}{2}\alpha h d_1 (x_1 - x_f)(x_f - x_1)$$
$$+ \frac{1}{2}\alpha h [d_1(x_1 - x_f) + 1](x_2 - x_f)$$
$$= \alpha h (x_2 - x_f)$$
$$= \left(\frac{\mathrm{d}p}{\mathrm{d}x}\right)^{-} |x_1 - x_f| + \left(\frac{\mathrm{d}p}{\mathrm{d}x}\right)^{+} |x_2 - x_f|$$
$$= \Delta p_{\mathrm{step}}, \tag{35}$$

where x_1 and x_2, respectively, represent the grid point ahead and behind the flame location, x_f, while $(\mathrm{d}p/\mathrm{d}x)^-$ and $(\mathrm{d}p/\mathrm{d}x)^+$ correspond to the values at the two ends of the step profile.

The non-conservative issue might not have occurred in studies on, for example, droplet and bubble dynamics, in which the singularity arises from surface tension. The global integration of the momentum equation recovers the boundary condition at the interface [24], whereby the pressure variation across the immersed zone is balanced

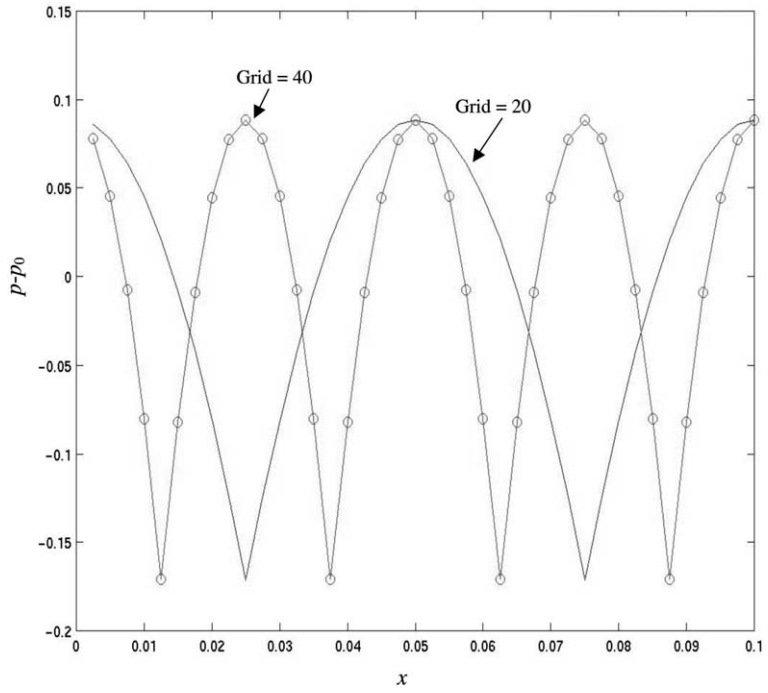

Fig. 6. The developed pressure (p_u) at the unburned (upstream) side of the flame front fails to converge to the analytical value if the cosine weighting function is used. It fluctuates periodically as the flame front moves within the cell, and the amplitude is independent of the mesh resolution.

by the specified surface tension. In the present situation, however, the singularity is generated by the divergence of mass flux, which needs to be computed as part of the solution.

There is an additional geometric requirement in the choice of the smoothing function, namely

$$h\sum_{j=1}^{n}\sum_{k=1}^{j} d_k(x_k - x_f) - \frac{1}{2} = \frac{|x_n - x_f|}{h}, \tag{36}$$

where x_f is chosen to lie in $[x_j, x_{j+1}]$. Eq. (36) simply states the equivalence of the numerical integration across the interface and the analytical distribution, which is a step function. It is exactly the integral in Eq. (34) derived from the error analysis. Alternatively, one can express the identity of the evaluations on both sides of the flame front, i.e.

$$\begin{aligned} &h\sum_{k=1}^{j-1}(|x_k - x_f| + |x_{k+1} - x_f|)d_k(x_k - x_f) + (x_j - x_f)^2 \\ &\quad \times d_j(x_j - x_f) = h\sum_{k=j+1}^{n}(|x_k - x_f| + |x_{k+1} - x_f|)d_k(x_k - x_f) \\ &\quad + (x_{j+1} - x_f)^2 d_j(x_j - x_f). \end{aligned} \tag{37}$$

Without satisfying Eq. (36) or Eq. (37), the pressure profile exhibits a periodic behavior corresponding to the relative front location, as shown in Figs. 4(a) and 6.

4. Propagation velocity of flame front

4.1. Oscillating flame propagation

The previous discussion is directed at the divergence of the mass flux embodying a given flame propagation velocity. In reality, the propagation velocity often needs to be evaluated based on the numerical solution of the flow field and the burning velocity of the mixture. In [19], averaged flow and flame velocities, obtained through interpolation, are used to calculate the movement of the interface. Specifically, the field properties at the interface are interpolated by using the δ-function, i.e.

$$\varphi(x_f) = \int_{\Omega} \varphi(x)\delta(x - x_f)\,\mathrm{d}x. \tag{38}$$

This is the inverse process of immersion in Eq. (9), which is evaluated for conservation in unit area (in 2-D), from the interface to the grid points. The discrete form leads to

$$\hat{\varphi}(x_f) = h\sum_j \hat{\varphi}_j(x_k) d_j(x_j - x_f). \tag{39}$$

However, we have found that substantial error is associated with such an interpolation process. The error accumulates in the course of iteration and can substantially degrade the solution accuracy. Together with the inaccuracy from the pressure calculation, such as that shown in Fig. 4(a), a large solution error results, as illustrated in Fig. 3(a).

To better understand this issue, we start from the correct velocity field, in which the divergence of the mass flux is evaluated with the aid of the area-weighting operator, Eq. (18). Then, we employ either Peskin's cosine weighting function or a linear (area) weighting function. As shown in Fig. 7(a), both treatments result in noticeable error, with the linear weighting function being worse. Furthermore, as shown in Fig. 7(b), the amplitude of the error is independent of the mesh resolution, indicating that the solution of the treatment based on [19] is only zeroth order accurate.

4.2. Error analysis

The interpolation involves approximating the interfacial variable by a discrete smoothing function, as shown in Eq. (39). Consider the mass flux ρu, designated as φ, which changes as a step function across the flame front. The value at the jump can be defined by the average, $(\varphi^+ + \varphi^-)/2$, which is described by the rigorous relation

$$\begin{aligned}\varphi(x) &= \varphi^- + H(x - x_f)(\varphi^+ - \varphi^-) \\ &= \frac{\varphi^+ + \varphi^-}{2} + \frac{\varphi^- - \varphi^+}{2} + (\varphi^+ - \varphi^-)H(x - x_f).\end{aligned} \tag{40}$$

The discrete step function can then be approximated as that for Eq. (30)

$$\begin{aligned}\hat{\varphi}_j(x_j) &= \frac{\varphi^+ + \varphi^-}{2} + \frac{\varphi^- - \varphi^+}{2} + (\varphi^+ - \varphi^-)\hat{H}_j(x_j - x_f), \\ \hat{H}_j(x_j - x_f) &= h\sum_k H(x_j - x_k) d_k(x_k - x_f).\end{aligned} \tag{41}$$

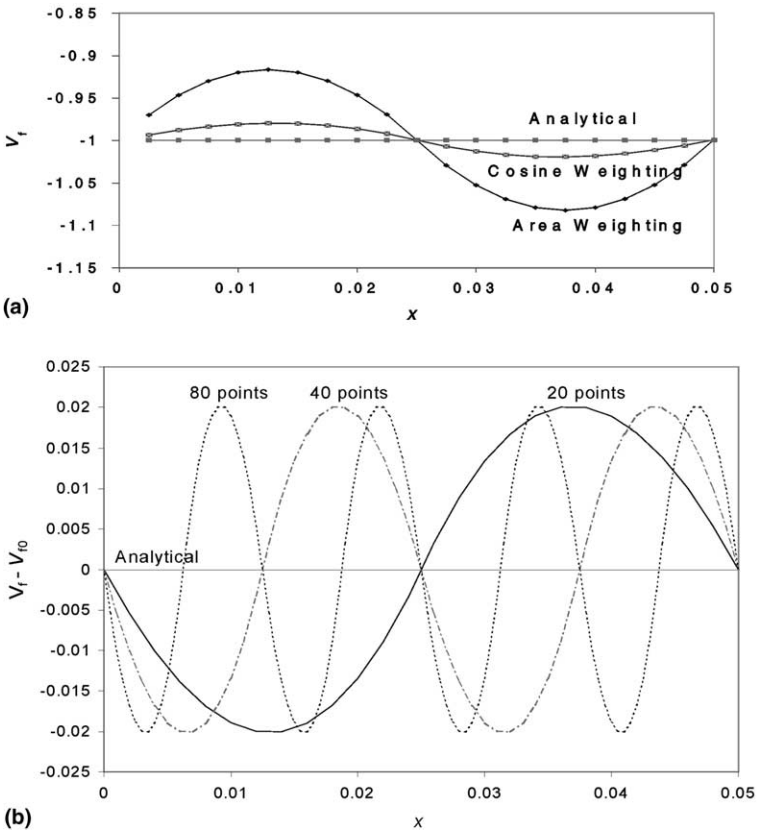

Fig. 7. The velocity of a flame front varies with its position relative to grid lines. (a) Different interpolations are compared with the analytical value. (b) The interpolation error is independent of mesh resolution but strongly correlates with the relative location of the flame front within a computational cell. For the case of 20 grids in domain size 1, the interval of 0.05 is a cycle for a marker to traverse a cell.

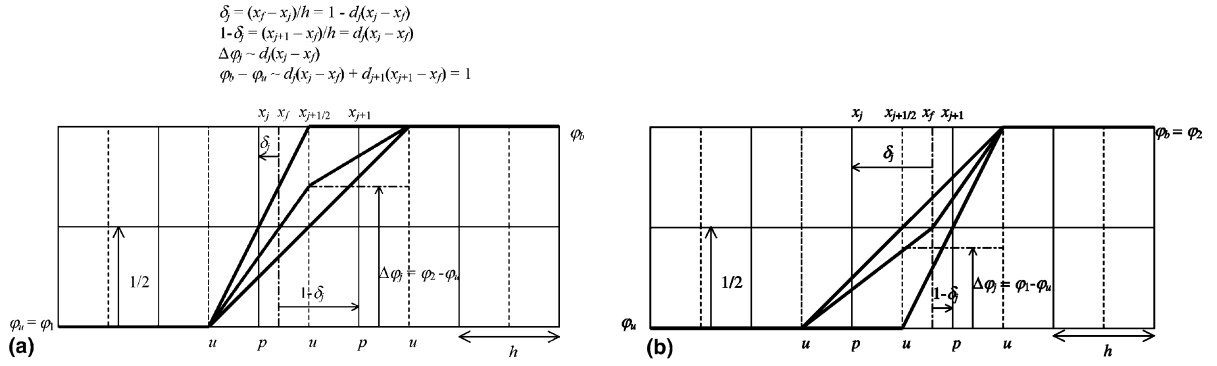

Fig. 8. Schematic of the recovering approach to interpolate the average mass flux at the interface. By linear weighting, a divergence of the mass flux at the interface is distributed to two surrounding grid points, whose quantity is proportional to the relative distance of the complementary part. Two structures are distinguished according to Eq. (44). (a) The flame front x_f is located between first and second velocity nodes, where $\varphi_1 = \varphi_u$ and φ_2. (b) x_f is located between second and third velocity nodes, where $\varphi_1 = \varphi(x_{j+1/2})$ and $\varphi_2 = \varphi_b$.

The discretization error then becomes

$$\begin{aligned}\hat{\varphi}(x_f) - \varphi(x_f) &= h\sum_j \hat{\varphi}_j(x_j)d_j(x_j - x_f) - \frac{\varphi^+ + \varphi^-}{2} \\ &= (\varphi^+ - \varphi^-)\left[h^2\sum_j\sum_k H(x_j - x_k)\right. \\ &\quad \left.\times d_k(x_k - x_f)d_j(x_j - x_f) - \frac{1}{2}\right] \\ &= (\varphi^+ - \varphi^-)h^2\sum_j\sum_k\left[H(x_j - x_k) - \frac{1}{2}\right] \\ &\quad \times d_k(x_k - x_f)d_j(x_j - x_f). \end{aligned} \tag{42}$$

Eq. (42) demonstrates that the error is periodic and O(1), which is consistent with that shown in Fig. 7. If φ is continuous and smooth, Beyer and LeVeque [3] have proven that the truncation error, for any smoothing function satisfying Eq. (8), is at most O(h). Second order accuracy can be attained if Eq. (26) is also satisfied. In the present situation, however, the average at the jump is to be approached, which is not associated with any distinct location in the immersed boundary. Therefore, as the front moves within a cell, the interpolation in Eq. (39) is influenced by the sweeping throughout the smoothed zone and periodic error occurs. As shown in Fig. 7(a), the performance of area weighting is less satisfactory than that of cosine weighting because it is interpolated by employing only two points, while the smoother distribution at four points carried by the latter can somehow moderate the spatial variation.

4.3. Improved approach

Based on the above discussion, it is clear that a satisfactory weighting function, in addition to Eqs. (8) and (26), needs to satisfy

$$\sum_j\sum_k H(x_j - x_k)d_k(x_k - x_f)d_j(x_j - x_f) = \frac{1}{2}. \tag{43}$$

We have developed a scheme, based on the area weighting function, to compute the mass flux, as shown in Fig. 8. Specifically, for a simple area weighting, the immersed boundary extends to only two cells connecting three velocity nodes (which are also used for mass flux computation) and the central value is proportional to the weight distributed to the contiguous pressure node ahead of the interface (on staggered grids). Divided by the weight, it recovers the difference between the two sides and the average at the jump can be obtained exactly. To accomplish this, we need to know the relation between the front location and three constituted velocity nodes. Two structures are sketched in Figs. 8(a) and (b). The averaged mass flux at the sharp interface can be calculated from the general form

$$\begin{aligned}\varphi_{1/2} &= \varphi_u + (\varphi_b - \varphi_u)H(x_p - x_f) + \frac{1}{2}\frac{\varphi_2 - \varphi_1}{d_p(x_p - x_f)} \\ &\quad \times [H(x_f - x_p) - H(x_p - x_f)], \end{aligned} \tag{44}$$

where φ_1 and φ_2 designate values at neighboring velocity nodes enclosing the interface, and x_p and $d_p(x_p - x_f)$ refer to the position and weight of the closest pressure node. These nodes can be found easily. By this analytical recovering, u_{ave} can almost approach the exact value, shown as the centerline in Fig. 7, with an error having an order around 10^{-10}.

5. Simulation of Darrieus–Landau instability

To demonstrate the applicability of the improved scheme in two-dimensional flows, we adopt the test problem of [8] and [19] for the evolution of Darri-

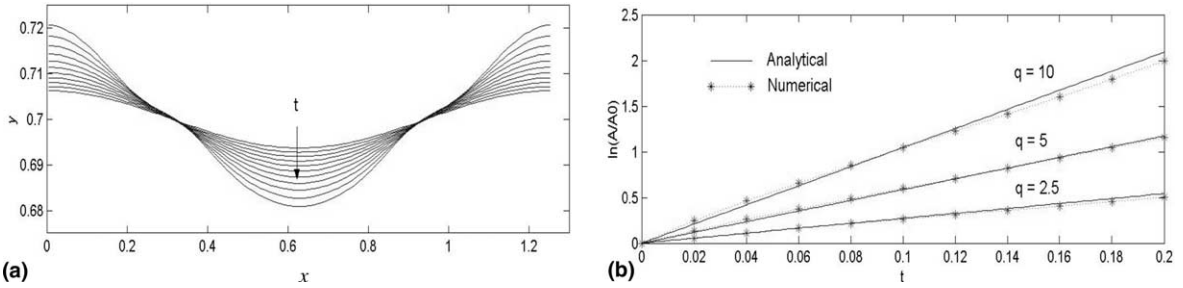

Fig. 9. The Darrieus–Landau instability simulation. (a) A sinusoidal perturbation of wave number $k = 5$ is initiated, with an amplitude 10^{-2} in unit of the wavelength, with a density ratio $q = 5$. The time of each curve corresponds to the "$*$" symbol in the lower graph. (b) The growth rate is compared in logarithmic scale to the analytical prediction.

eus–Landau (hydrodynamic) instability [12]. Separating two media with different densities and under the condition that the laminar burning velocity is constant, the flame front is inherently unstable. From linear stability analysis [13], the growth rate of a perturbation to a planar flame is given by

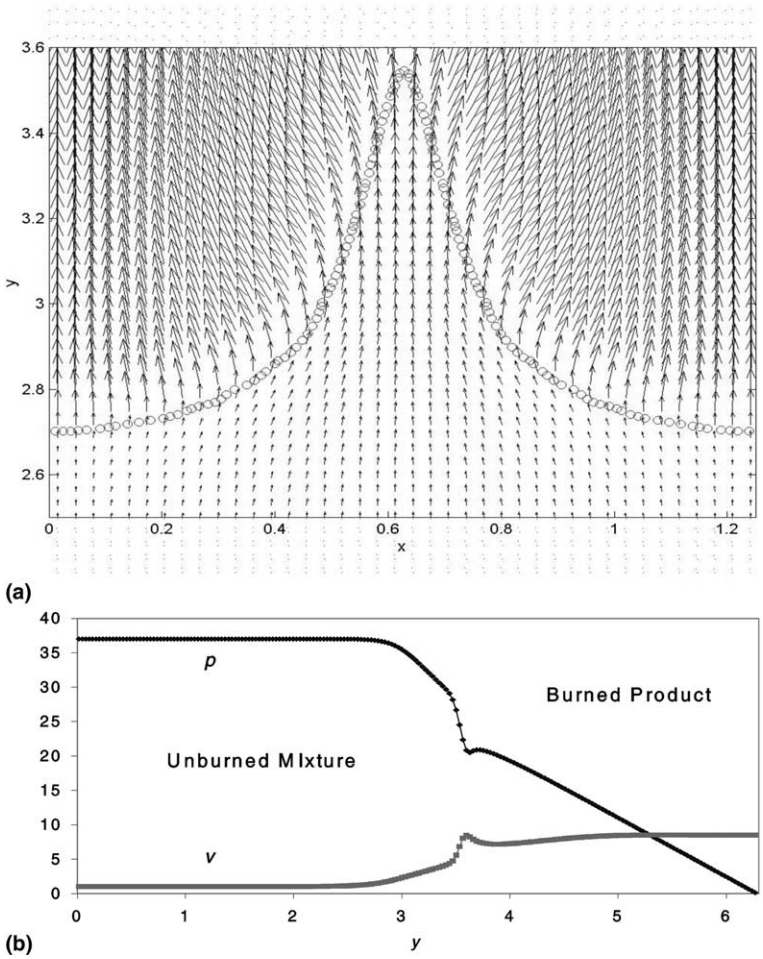

Fig. 10. The flow field at a later time ($t = 0.2$) after initially perturbed with a large sinusoidal wave (Amp. $= 0.2, q = 5$) resolved by 40×200 grid points. (a) Velocity vectors across the flame front. (b) Profiles of the pressure and velocity (v component) along the centerline in y direction.

$$\omega = \frac{km/\rho_b}{1+q}\left[-1+\left(1+q-\frac{1}{q}\right)^{1/2}\right], \tag{45}$$

where k is the wave number, q the density ratio of unburned (ρ_u) to burned gases (ρ_b), and m is the mass flux with a dimensionless value of unity.

The parameters adopted here are identical to those used in [19], with $\rho_u = 1$, $\rho_b = 0.2$ (for $q = 5$), $\mu_u = 0.011$, $\mu_b = 0.035$, and $s_u = 1$. These values are based on methane/air flame propagation at atmospheric conditions. An inlet flow with unity speed is inputted to anchor the flame evolution at the center of the computational domain. Before launching the front development, the steady-state solution corresponding to the original flame configuration is obtained to serve as the initial flow field. Fig. 9 shows the evolution of a sinusoidal wave initially triggered with an amplitude of 10^{-2} in unit of the wavelength in $[2\pi/5, 2\pi/5]$ resolved by 60×60 grid points. Various density ratios are implemented. The numerical trend agrees well with the linear analytical prediction. Nonlinear effects, however, reduce the agreement at later times, particularly for higher density jumps associated with larger growth rates.

The numerical error is aggravated by hydrodynamic instability, especially for large-amplitude disturbances. In order to minimize the numerical instability, we have adopted a smoother area weighting by four points [3] to simulate the evolution of a perturbation with large amplitude

$$d(r) = \begin{cases} \frac{1}{4h}(2-|r|/h), & |r| \leqslant 2h, \\ 0, & |r| \geqslant 2h, \end{cases} \tag{46}$$

where the staggered set of two points share half of the total weight so that Eq. (8) can be satisfied. Meanwhile, Eq. (26) can be satisfied as well and no error for pressure computation is introduced. A similar evaluation as Eq. (44) for the interface velocity based on four grid points has been employed.

To eliminate the influence from the boundary conditions in the finite domain for the present problem of flame evolution with significant topological variations, the computation is performed in a domain with ex-

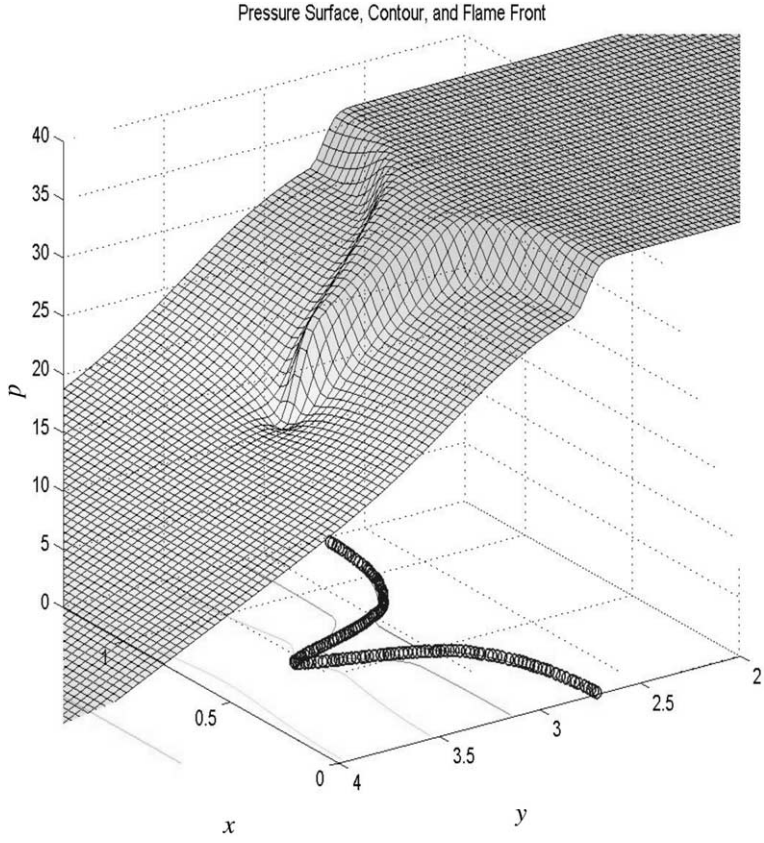

Fig. 11. The pressure field at a later time ($t = 0.2$) after initially perturbed with a large sinusoidal wave (Amp. $= 0.2, q = 5$). The corresponding contours and flame front are projected on the bottom plane.

tended size in the propagation direction (y), e.g., in $[2\pi/5, 2\pi]$. It ensures that no spatial variation in the transverse direction (x) is introduced at the Dirichlet boundary with $p = 0$. The results are shown in Figs. 10 and 11 for the velocity and pressure profiles. The velocity vectors (Fig. 10(a)) illustrate convergence of the flow toward the cusp and the subsequent divergence downstream of the flame, conserving mass flux upon gas expansion. The corresponding pressure field is shown in Fig. 11, which depicts a decreasing trend through contraction of the flow passage toward the cusp. The profiles along the centerline (Fig. 10(b)) reveal an extremum at the cusp, which results from the convergent–divergent characteristic of the streamline. The negative pressure gradient in the burned region demonstrates the significance of the unsteady effects of the flow, excited by substantial growth of the hydrodynamic instability.

6. Conclusions

Accuracy of the immersed-boundary method for simulating the dynamics of premixed flame has been analyzed and improved. To account for the jumps in pressure and velocity profiles across the flame, the proposed treatment satisfies the geometric conservation laws to prevent the appearance of spurious solutions in the pressure field caused by the moving front. A numerical analysis is presented to evaluate the performance of alternate smoothing functions. It is shown that area weighting prevents pressure oscillations while cosine weighting is inherently prone to such an error.

Furthermore, it is demonstrated that since flame propagation requires evaluation of the local flow velocity at the sharp interface, use of the conventional procedure, with either the cosine or area weighting function, introduces errors of $O(1)$. An improved method based on the known immersion distribution is proposed, yielding the appropriate propagation velocity at the front with the discontinuous velocity profile. The modified scheme has been tested for steady and unsteady planar flame propagation, as well as the evolution of Darrieus–Landau instability. Satisfactory results are obtained, indicating that the improved treatments proposed herein can properly describe fluid flows involving moving fronts and property jumps.

Acknowledgements

C.K. Law's and W. Shyy's efforts have been supported by AFOSR and Eglin AFB, respectively.

References

[1] K.M. Arthurs, L.C. Moore, C.S. Peskin, E.B. Pitman, H.E. Layton, Modeling arteriolar flow and mass transport using the immersed boundary method, J. Comput. Phys. 147 (1998) 402.
[2] J.U. Brackbill, D.B. Kothe, C. Zemach, A continuum method for modeling surface tension, J. Comput. Phys. 100 (1992) 335.
[3] R.P. Beyer, R.J. Leveque, SIAM J. Numer. Anal. 29 (1992) 332.
[4] A.J. Chorin, Flame advection and propagation algorithms, J. Comput. Phys. 35 (1980) 1.
[5] L.J. Fauci, C.S. Peskin, A computational model of aquatic animal locomotion, J. Comput. Phys. 77 (1988) 85.
[6] R. Fedkiw, T. Aslam, B. Merriman, S. Osher, A non-oscillatory Eulerian approach to interfaces in multimaterial flows (the ghost fluid method), J. Comput. Phys. 152 (1999) 457.
[7] F.H. Harlow, J.E. Welch, Numerical calculation of time-dependent viscous incompressible flow of fluid with free surface, Phys. Fluids 8 (1965) 2182.
[8] B.T. Helenbrook, L. Martinelli, C.K. Law, A numerical method for solving incompressible flow problems with a surface of discontinuity, J. Comput. Phys. 148 (1999) 366.
[9] T.Y. Hou, J.S. Lowengrub, M.J. Shelley, Boundary integral methods for multicomponent fluids and multiphase materials, J. Comput. Phys. 169 (2001) 302.
[10] D. Juric, G. Tryggvason, Computations of boiling flows, Int. J. Multiphase Flow 24 (1998) 387.
[11] M.-C. Lai, C.S. Peskin, An immersed boundary method with formal second-order accuracy and reduced numerical viscosity, J. Comput. Phys. 160 (2000) 705.
[12] L.D. Landau, E.M. Lifshitz, Fluid Mechanics, second ed., Butterworth–Heinemann, Oxford, 1987.
[13] M. Matalon, B.J. Matkowsky, Flames as gasdynamic discontinuities, J. Fluid Mech. 124 (1982) 239.
[14] D.Q. Nguyen, R.P. Fedkiw, M. Kang, A boundary condition capturing method for incompressible flame discontinuities, J. Comput. Phys. 172 (2001) 71.
[15] W. Noh, P. Woodward, Simple line interface calculation, in: Lecture Notes in Physics, vol. 59, Springer, New York/Berlin, 1976, p. 330.
[16] S. Osher, R.P. Fedkiw, Level set methods: an overview and some recent results, J. Comput. Phys. 169 (2001) 463.
[17] C.S. Peskin, Numerical analysis of blood flow in the heart, J. Comput. Phys. 25 (1977) 220.
[18] C.S. Peskin, B.F. Printz, Improved volume conservation in the computation of flows with immersed elastic boundaries, J. Comput. Phys. 105 (1993) 33.
[19] J. Qian, G. Tryggavason, C.K. Law, A front tracking method for the motion of premixed flames, J. Comput. Phys. 144 (1998) 52.
[20] R. Peyret, T.D. Taylor, Computational Methods for Fluid Flows, Springer, New York/Berlin, 1983.
[21] R. Scardovelli, S. Zaleski, Direct numerical simulation of free-surface and interfacial flow, Annu. Rev. Fluid Mech. 31 (1999) 567.

[22] J.A. Sethian, Level Set Methods, Cambridge University Press, Cambridge, MA, 1996.
[23] W. Shyy, H.S. Udaykumar, M.M. Rao, R.W. Smith, Computational Fluid Dynamics with Moving Boundaries, Taylor & Francis, Washington, DC, 1996.
[24] G. Tryggvason, B. Bunner, A. Esmaeeli, D. Juric, N. Al-Rawahi, W. Tauber, J. Han, S. Nas, Y.-J. Jan, A front-tracking method for the computations of multiphase flow, J. Comput. Phys. 169 (2001) 708.
[25] H.S. Udaykumar, H.-C. Kan, W. Shyy, R. Tran-Son-Tray, Multiphase dynamics in arbitrary geometries on fixed Cartesian grids, J. Comput. Phys. 137 (1997) 366.
[26] W. Shyy, M. Francois, H.S. Udaykumar, N. N'dri, R. Tran-Son-Tay, Moving boundaries in micro-scale biofluid dynamics, Appl. Mech. Rev. 54 (2001) 419.
[27] S.O. Unverdi, G. Tryggvason, A front-tracking method for viscous incompressible multi-fluid flows, J. Comput. Phys. 100 (1992) 25.
[28] M.W. Williams, D.B. Kothe, E.G. Puckett, Accuracy and convergence of continuum surface-tension models, in: W. Shyy, R. Narayanan (Eds.), Fluid Dynamics at Interfaces, Cambridge, 1999 (Chapter 23).
[29] T. Yabe, F. Xiao, T. Utsumi, The constrained interpolation profile method for multiphase analysis, J. Comput. Phys. 169 (2001) 556.